

Plug-and-Hide: Provable and Adjustable Diffusion Generative Steganography

JIAHAO ZHU, School of Computer Science and Engineering, Sun Yat-sen University, China
ZIXUAN CHEN, School of Computer Science and Engineering, Sun Yat-sen University, China
JIALI LIU, Zhongshan School of Medicine, Sun Yat-sen University, China
WEIQI LUO, School of Computer Science and Engineering, Sun Yat-sen University, China
YI ZHOU*, Zhongshan School of Medicine, Sun Yat-sen University, China
XIAOHUA XIE*, School of Computer Science and Engineering, Sun Yat-sen University, China

Diffusion model-based generative image steganography (DM-GIS) is an emerging paradigm that leverages the generative power of diffusion models to conceal secret messages without requiring pre-existing cover images. In this paper, we identify a fundamental trade-off between stego image quality, steganographic security, and extraction reliability within the DM-GIS framework. Drawing on this insight, we propose **PA-B2G**, a **Provable and Adjustable Bit-to-Gaussian** mapping. Theoretically, PA-B2G guarantees the reversible encoding of arbitrary-length bit sequences into pure Gaussian noise; practically, it enables fine-grained control over the balance between image fidelity, security, and extraction accuracy. By integrating PA-B2G with probability-flow ordinary differential equations (PF-ODEs), we establish a theoretically invertible mapping between secret bitstreams and stego images. PA-B2G is model-agnostic and can be seamlessly integrated into mainstream diffusion models without additional training or fine-tuning, making it also suitable for diffusion model watermarking. Extensive experiments validate our theoretical analysis of the inherent DM-GIS trade-offs and demonstrate that our method flexibly supports arbitrary payloads while achieving competitive image quality and security. Furthermore, our method exhibits strong resilience to lossy processing in watermarking applications, highlighting its practical utility.

ACM Reference Format:

Jiahao Zhu, Zixuan Chen, Jiali Liu, Weiqi Luo, Yi Zhou, and Xiaohua Xie. 2026. Plug-and-Hide: Provable and Adjustable Diffusion Generative Steganography. 1, 1 (March 2026), 18 pages. <https://doi.org/10.1145/nnnnnnn.nnnnnnn>

1 Introduction

Steganography, as both an art and a science, aims to conceal secret data within seemingly innocuous carriers such as images for covert communication [6, 22]. In traditional image steganography, benign images (*a.k.a.* cover images) are usually selected as message carriers, and secret messages are embedded into their least significant bits using either non-adaptive embedding schemes [16] or

Authors' Contact Information: Jiahao Zhu, zhujh59@mail2.sysu.edu.cn, School of Computer Science and Engineering, Sun Yat-sen University, Guangzhou, Guangdong, China; Zixuan Chen, chenxz3@mail2.sysu.edu.cn, School of Computer Science and Engineering, Sun Yat-sen University, Guangzhou, Guangdong, China; Jiali Liu, 18879466196@163.com, Zhongshan School of Medicine, Sun Yat-sen University, Guangzhou, Guangdong, China; Weiqi Luo, luoweiqi@mail.sysu.edu.cn, School of Computer Science and Engineering, Sun Yat-sen University, Guangzhou, Guangdong, China; Yi Zhou, luoweiqi@mail.sysu.edu.cn, Zhongshan School of Medicine, Sun Yat-sen University, Guangzhou, Guangdong, China; Xiaohua Xie, xiexiah6@mail.sysu.edu.cn, School of Computer Science and Engineering, Sun Yat-sen University, Guangzhou, Guangdong, China.

Permission to make digital or hard copies of all or part of this work for personal or classroom use is granted without fee provided that copies are not made or distributed for profit or commercial advantage and that copies bear this notice and the full citation on the first page. Copyrights for components of this work owned by others than the author(s) must be honored. Abstracting with credit is permitted. To copy otherwise, or republish, to post on servers or to redistribute to lists, requires prior specific permission and/or a fee. Request permissions from permissions@acm.org.

© 2026 Copyright held by the owner/author(s). Publication rights licensed to ACM.

ACM XXXX-XXXX/2026/3-ART

<https://doi.org/10.1145/nnnnnnn.nnnnnnn>

adaptive embedding strategies [1]. However, such algorithms generally suffer from limited message embedding capacity. Moreover, even at low payloads, message concealment inevitably introduces statistical discrepancies between cover images and their corresponding stego images, increasing the risk of being detected by machine learning-based steganalysis methods [2, 26, 30, 32].

To address these challenges, generative image steganography has emerged as a promising solution. Different from traditional image steganography, generative image steganography employs generative models to directly synthesize stego images from secret messages, thus avoiding the need for pre-defined cover carriers. Early approaches [5, 12, 13, 17, 25, 27, 28, 33, 36, 37] are mainly built upon Generative Adversarial Networks (GANs) [3] and Flow models [10]. GAN-based methods [5, 12, 13, 17, 25, 27, 33, 36] usually require three collaborative networks: a generator, a discriminator, and a message extractor. This demands a delicate trade-off between image generation and message extraction during training, which raises training complexity and often results in unsatisfactory visual quality and message extraction accuracy. In contrast, flow-based methods [28, 37] exploit the strict reversibility of flow models to establish a bijective mapping between secret messages and images. Nevertheless, this inherent reversibility constrains their performance in high-resolution image generation.

Recent studies [7, 9, 31, 35] leverage pre-trained image diffusion models [19–21] for generative steganography. These methods typically follow a two-step pipeline: the first is an invertible bit-to-noise mapping that transforms secret bits into Gaussian or quasi-Gaussian noise; the second is stego image generation from the noise by solving a probability flow ordinary differential equation (PF-ODE) with solvers such as DPM-Solvers [14, 15, 34]. However, existing diffusion model-based generative image steganography (DM-GIS) methods struggle to flexibly support arbitrary-length secret payloads while simultaneously maintaining high message extraction accuracy, stego image quality, and steganographic security. Specifically, approaches in [7, 31, 35] achieve high extraction reliability and image fidelity but are limited to low effective payloads, which restricts their practicality. Diffusion-Stego [9] supports both low and high payloads but at the expense of compromised security and image quality. These limitations reveal two fundamental issues that remain underexplored: the intrinsic relationship among stego image quality, steganographic security, and message extraction accuracy, as well as the challenge of achieving an optimal trade-off among them. Although Kim *et al.* empirically identifies a trade-off between image quality and extraction accuracy in DM-GIS [9], it overlooks the critical dimension of steganographic security.

In this paper, we theoretically elucidate the underlying relationship among stego image quality, extraction accuracy, and steganographic security in DM-GIS, which is under-explored in previous studies. We identify that the key to balancing these three factors lies in the Gaussianity of the noise generated from secret bits. Specifically, DM-GIS methods that compromise Gaussianity are prone to producing sub-optimal stego images and achieving inferior security. Given a fixed encoding scheme and effective payload, pursuing higher message extraction accuracy inevitably impairs Gaussianity, thereby degrading generation quality and security. Based on these findings, we propose a provable and adjustable bit-to-Gaussian mapping, named PA-B2G, which reversibly transforms bit sequences of arbitrary length into pure Gaussian noise. PA-B2G consists of two stages: **i**) mapping bitstreams to uniformly sampled noise using a symmetric interval partitioning strategy; and **ii**) generating pure Gaussian noise via inverse transform sampling. Furthermore, we introduce non-sampling intervals and a variance-preserving adjustable algorithm, which enables fine-grained control over generation quality, security, and extraction accuracy. By iteratively denoising the noise generated by PA-B2G with an ODE solver, we establish a theoretically invertible mapping between secret messages and stego images. This approach allows PA-B2G to be integrated into most mainstream diffusion models without additional training or fine-tuning. Consequently, our method can be effectively extended to diffusion model watermarking.

The main contributions of this work are summarized as follows:

- We propose PA-B2G, which can provably and reversibly transform arbitrary-length bit sequences into standard Gaussian noise. Its adjustability enables a flexible and fine-grained trade-off among stego image quality, steganographic security, and message extraction accuracy.
- PA-B2G decouples message embedding, stego image generation, and message extraction, which facilitates its direct integration into off-the-shelf diffusion models without any training or fine-tuning, thus realizing plug-and-hide functionality.
- Experiments demonstrate that our method supports arbitrary-length payloads while achieving competitive stego image quality and steganographic security. Moreover, its resilience to lossy processing in watermarking highlights its practical utility.

The remainder of this paper is organized as follows. Section 2 reviews existing DM-GIS algorithms. Section 3 introduces preliminary knowledge of PF-ODE in diffusion models. Section 4 analyzes the relationship among stego image quality, steganographic security, and message extraction accuracy, and presents our provable and adjustable PA-B2G mapping. Section 5 reports the experimental results. Section 6 concludes this work and discusses its limitations.

2 Related Work

GIS is a novel technique that conceals secret messages within synthesized images using generative models. It can be broadly categorized into three classes:

GAN-based Methods. Liu *et al.* [12] pioneered GAN-based steganography by replacing class labels with secret data to synthesize stego images. Hu *et al.* [5] employed GANs to convert secret data into noise vectors for generating carrier images. Wang *et al.* [25] introduced a self-learning GAN-based approach for direct stego image generation from secret messages. Yu *et al.* [33] proposed an attention-GAN method with optimized network architecture and loss functions. Despite these improvements, such methods still suffer from issues including low image quality and unsatisfactory message extraction accuracy. To address these problems, Liu *et al.* [13] introduced an image disentanglement autoencoder for generative steganography, which improves both visual quality and extraction accuracy. Wei *et al.* [27] incorporated a mutual information mechanism to enhance extraction accuracy and designed a hierarchical gradient decay strategy to strengthen anti-steganalysis performance. To tackle robustness problems in message recovery and synthesis quality, Ma *et al.* [17] developed a weight modulation-based generator and a difference predictor to improve extraction robustness. Most recently, Zhou *et al.* [36] identified security vulnerabilities in the feature domain of existing GAN-based generative steganography schemes. They further proposed a framework that automatically generates semantic object contours to enhance steganographic security.

Flow-based Methods. To achieve higher embedding capacity and improved message extraction accuracy, Wei *et al.* [28] proposed a novel flow-based generative steganography algorithm, which directly embeds secret messages into the binarized initial noise of a pre-trained Glow model [10]. In a similar vein, Zhou *et al.* [37] proposed Secret-to-Image Reversible Transformation (S2IRT), which incorporates the idea of permutation steganography permutation to encode secret bits by rearranging the order of entries in the latent vectors of Glow.

Diffusion Model-based Methods. With the advent of diffusion models, Peng *et al.* [18] proposed StegaDDPM, a novel DM-GIS algorithm based on the denoising diffusion probabilistic model (DDPM) [4]. StegaDDPM embeds secret information by exploiting the probability distribution between the intermediate states and generated images of DDPM. Yang *et al.* [31] presented a provably secure bit-to-Gaussian mapping method using distribution-preserving sampling. Hu *et al.*

[7] introduced a novel bit-to-Gaussian mapping module based on orthogonal matrices and dual keys. Zhou *et al.* [35] proposed a scheme named generative steganography diffusion (GSD) that conceals secret bits in the frequency domain of the initial Gaussian noise. Kim *et al.* [9] designed four message projection strategies—Message to Noise (MN), Message to Binary (MB), Message to Centered Binary (MC), and Multi-bits—to balance image quality and message extraction performance.

3 Preliminary

Recent studies [4, 8, 23, 24] have demonstrated that visually plausible generated images can be obtained by iteratively denoising pure Gaussian noise. This denoising process can be modeled by the following PF-ODE [8, 24]:

$$d\mathbf{x} = \left[\mathbf{f}(\mathbf{x}, t) - \frac{1}{2}g(t)^2 \nabla_{\mathbf{x}} \log p_t(\mathbf{x}) \right] dt, \quad (1)$$

where $f(\mathbf{x}, t)$ and $g(t)$ denote the drift term and diffusion coefficient with respect to timestep t , respectively. $\nabla_{\mathbf{x}} \log p_t(\mathbf{x})$ denotes the score function [24], which points to the direction of higher probability density of the data \mathbf{x} and is usually approximated by a deep neural network $\frac{1}{\sigma_t} \epsilon_{\theta}(\mathbf{x}, t)$. Assuming that the integration interval of Equation (1) is set to $[0, T]$, an image \mathbf{x}_0 can be generated by integrating Equation (1) from time T to 0; similarly, \mathbf{x}_T can be recovered by integrating Equation (1) along the reverse time direction. These two computational paths are fully invertible [11]. In practice, the integral associated with the denoising process can be approximately solved using off-the-shelf ODE solvers (e.g., the Euler method [23] and DPM-Solvers [14, 34]) by iteratively denoising pure Gaussian noise $\mathbf{x}_T \sim \mathcal{N}(\mathbf{0}, \sigma_T^2 \mathbf{I})$. This process can be expressed as:

$$\mathbf{x}_{t-1} = \mathbf{x}_t + \int_t^{t-1} \left(f(t)\mathbf{x}_t + \frac{g(t)^2}{2\sigma_t} \epsilon_{\theta}(\mathbf{x}_t, t) \right) dt, \quad (2)$$

Likewise, \mathbf{x}_T can be approximately recovered by reversing this process. In this paper, we leverage high-order ODE solvers, such as the second-order Heun solver [8] and DPM-Solver-2 [14], since they introduce smaller local errors.

4 Our Method

In Section 4.1, we revisit the fundamental trade-off between stego image quality and message extraction accuracy, originally identified by Kim *et al.* [9], and further incorporate a discussion of steganographic security. Building upon this analysis, we introduce the PA-B2G mapping in Section 4.2 and its adjustable variant in Section 4.3. The detailed message hiding and extraction processes are then presented in Section 4.4.

4.1 Theoretical Analysis

What Shapes Stego Image Quality and Security? Let \mathbf{g}_s and \mathbf{g} denote the noise generated by DM-GIS and pure Gaussian noise, respectively, and let \mathbf{x}_s and \mathbf{x} denote the corresponding images generated by the diffusion model with parameter θ . According to Theorem 1 proposed in [38], we have

$$D_{\text{KL}}(p(\mathbf{g}_s) \parallel p(\mathbf{g})) = D_{\text{KL}}(p_{\theta}(\mathbf{x}_s) \parallel p_{\theta}(\mathbf{x})). \quad (3)$$

The optimization objective of diffusion models can be fundamentally formulated via maximum likelihood estimation [4] and KL divergence, as follows:

$$-E_{p_{\text{data}}} [\log p_{\theta}(\mathbf{x})] = D_{\text{KL}}(p_{\text{data}}(\mathbf{x}) \parallel p_{\theta}(\mathbf{x})) + H(p_{\text{data}}(\mathbf{x})), \quad (4)$$

where p_{data} and p_{θ} denote the real image distribution and the learned image distribution, respectively, and $H(\cdot)$ denotes the entropy function. Equation (4) implies that for a well-trained diffusion model,

$D_{\text{KL}}(p_{\text{data}} \parallel p_{\theta}) = 0$. Combined with Equation (3), we theoretically obtain

$$D_{\text{KL}}(p(\mathbf{g}_s) \parallel p(\mathbf{g})) = D_{\text{KL}}(p_{\theta}(\mathbf{x}_s) \parallel p_{\text{data}}(\mathbf{x})). \quad (5)$$

Equation (5) reveals that the Gaussianity of \mathbf{g}_s directly affects the stego image quality as well as the steganographic security (see [38] for details). To achieve perfect stego image generation and security, one must ensure that \mathbf{g}_s follows a pure Gaussian distribution. Any steganographic operation that compromises the Gaussianity will theoretically degrade both visual quality and security.

What Shapes Message Extraction Accuracy? As analyzed in [38], given a fixed encoding scheme and effective payload, one has to compromise the Gaussianity of \mathbf{g}_s , such as the adjustment schemes adopted in Diffusion-Stego [9] and S2IRT [37], to achieve higher message extraction accuracy. This inevitably compromises both generation quality and security, as demonstrated in Equation (5). Notably, to mitigate the destruction of Gaussianity, S2IRT employs an additional perturbation key in its message encoding function, which essentially breaks the constraint of “under the same steganography encoding”.

4.2 Design of PA-B2G

As demonstrated in Section 4.1, achieving perfect generation quality and security requires that the generated noise \mathbf{g}_s be strictly Gaussian noise. To this end, we design a provably invertible bit-to-Gaussian mapping, termed PA-B2G, which comprises two stages. In the first stage, to handle secret bits with arbitrary lengths, the encrypted bit sequence $\mathbf{b} = b_1 b_2 \cdots b_n$ is divided into several subsequences of length l , forming an integer sequence $\mathbf{m} = m_1 m_2 \cdots m_k$ with $m_i \in \{0, 1, \dots, 2^l - 1\}$. Then, the integer sequence \mathbf{m} is transformed into uniformly distributed noise $\mathbf{u} = u_1 u_2 \cdots u_k$, which can be defined by $C_u(\mathbf{m}) = \mathbf{u}$. Inspired by arithmetic coding, we leverage a symmetrical interval partitioning strategy and introduce the following two partition modes:

- I. The interval $[0, 1]$ is evenly partitioned into 2^l , and u_i is sampled from $\mathcal{U}(\frac{m_i}{2^l}, \frac{m_i+1}{2^l})$.
- II. The interval $[0, 1]$ is evenly partitioned into 2^{l+1} , and u_i is sampled from $\mathcal{U}(\frac{m_i}{2^{l+1}}, \frac{m_i+1}{2^{l+1}})$ or $\mathcal{U}(1 - \frac{m_i+1}{2^{l+1}}, 1 - \frac{m_i}{2^{l+1}})$.

In the second stage, the obtained sequence \mathbf{u} is transformed into pure Gaussian noise by the inverse transform sampling, which is defined by $\mathbf{g}_s = C_g(\mathbf{u})$. C_g is also known as the percent point function (PPF) *w.r.t.* $\mathcal{N}(0, 1)$. The implementation details of PA-B2G and its inverse procedure are provided in Algorithm 1 and Algorithm 2, respectively. Note that intervals partitioned by the two modes are all symmetric about $u = \frac{1}{2}$, which is the reason we refer to our method as the symmetrical interval partition, and its rationale is discussed in the next section.

In practice, we can replicate and concatenate the secret message to generate the Gaussian noise \mathbf{g}_s . This approach essentially leverages repetition coding to improve extraction accuracy at the expense of effective embedding capacity. Consequently, as shown in Section 5.4, this trade-off is particularly suitable for diffusion model watermarking.

Here we first demonstrate the Gaussianity of the generated noise \mathbf{g}_s .

THEOREM 4.1. *Given a message sequence $\mathbf{m} = m_1 m_2 \cdots m_k$, $\mathbf{g}_s = C_g \circ C_u(\mathbf{m}) \sim \mathcal{N}(\mathbf{0}, \mathbf{I})$.*

PROOF. $p(\mathbf{g}) = \sum_m p(\mathbf{g}|\mathbf{m})p(\mathbf{m})$. Since \mathbf{m} is encrypted beforehand, $p(\mathbf{m}) = 2^{-l}$, and

$$\begin{aligned} p(\mathbf{g}|\mathbf{m}) &= \int p(\mathbf{g}, \mathbf{u}|\mathbf{m})d\mathbf{u} = \int p(\mathbf{g}|\mathbf{u}, \mathbf{m})p(\mathbf{u}|\mathbf{m})d\mathbf{u} \\ &= p(\mathbf{g}|C_u(\mathbf{m}))p(C_u(\mathbf{m})). \end{aligned} \quad (6)$$

Algorithm 1 PA-B2G**Input:** Secret message \mathbf{m} .**Output:** Pure Gaussian noise \mathbf{g} .

- 1: **for** $i = 1$ to k **do**
- 2: Sample $r_i \sim \mathcal{U}(0, 1)$;
- 3: $u_i = \frac{r_i}{2^l} + \frac{m_i}{2^l}$; \triangleright mode I
- 4: $u_i = \frac{r_i}{2^{l+1}} + \frac{m_i}{2^{l+1}}$ or $u_i = \frac{r_i}{2^{l+1}} + 1 - \frac{m_i+1}{2^{l+1}}$; \triangleright mode II
- 5: $g_i = C_g(u_i)$;
- 6: $\mathbf{g} = g_1 g_2 \cdots g_k$;
- 7: **Return** \mathbf{g} .

Algorithm 2 Inverse Procedure of PA-B2G**Input:** Noise \mathbf{g} .**Output:** Secret message \mathbf{m} .

- 1: **for** $i = 1$ to k **do**
- 2: $u_i = C_g^{-1}(g_i)$;
- 3: $m_i = \lfloor u_i 2^l \rfloor$; \triangleright mode I
- 4: $m_i = \lfloor (1 - u_i) 2^{l+1} \rfloor$ **if** $u_i > 0.5$ **else** $\lfloor u_i 2^{l+1} \rfloor$; \triangleright mode II
- 5: $\mathbf{m} = m_1 m_2 \cdots m_k$;
- 6: **Return** \mathbf{m} .

For the mode I,

$$\begin{aligned}
 p(g|m) &= p(g|C_u(m))p(C_u(m)) = \frac{2^l p(g|C_u(m))}{(m+1-m)} \\
 &= \begin{cases} \frac{2^l}{\sqrt{2\pi}} e^{-\frac{g^2}{2}} & \text{if } g \in [C_g(\frac{m}{2^l}), C_g(\frac{m+1}{2^l})] \\ 0 & \text{otherwise.} \end{cases} \tag{7}
 \end{aligned}$$

According to Equation (6),

$$\begin{aligned}
 p(g) &= p(g|m)p(m) = \frac{1}{2^l} \sum_m p(g|m)p(m) \\
 &= \sum_m p(g|C_u(m)) = \frac{1}{\sqrt{2\pi}} e^{-\frac{g^2}{2}} := \mathcal{N}(0, 1), g \in \mathbb{R}. \tag{8}
 \end{aligned}$$

For the mode II,

$$\begin{aligned}
 p(g|m) &= p(g|C_u(m))p(C_u(m)) = \frac{2^{l+1} p(g|C_u(m))}{2(m+1-m)} \\
 &= \begin{cases} \frac{2^l}{\sqrt{2\pi}} e^{-\frac{g^2}{2}} & \text{if } g \in [C_g(\frac{m}{2^{l+1}}, C_g(\frac{m+1}{2^{l+1}})], \\ \frac{2^l}{\sqrt{2\pi}} e^{-\frac{g^2}{2}} & \text{if } g \in [C_g(1 - \frac{m+1}{2^{l+1}}, C_g(1 - \frac{m}{2^{l+1}})], \\ 0 & \text{otherwise.} \end{cases} \tag{9}
 \end{aligned}$$

similarly, we can obtain $p(g) = \frac{1}{\sqrt{2\pi}} e^{-\frac{g^2}{2}} := \mathcal{N}(0, 1)$, where $g \in \mathbb{R}$. Since g_i are *i.i.d.*, $p(\mathbf{g}) = \prod_{i=1}^k p(g_i) = \frac{1}{(2\pi)^{k/2}} e^{-\frac{1}{2}\mathbf{g}^T \mathbf{g}} := \mathcal{N}(\mathbf{0}, \mathbf{I})$. \square

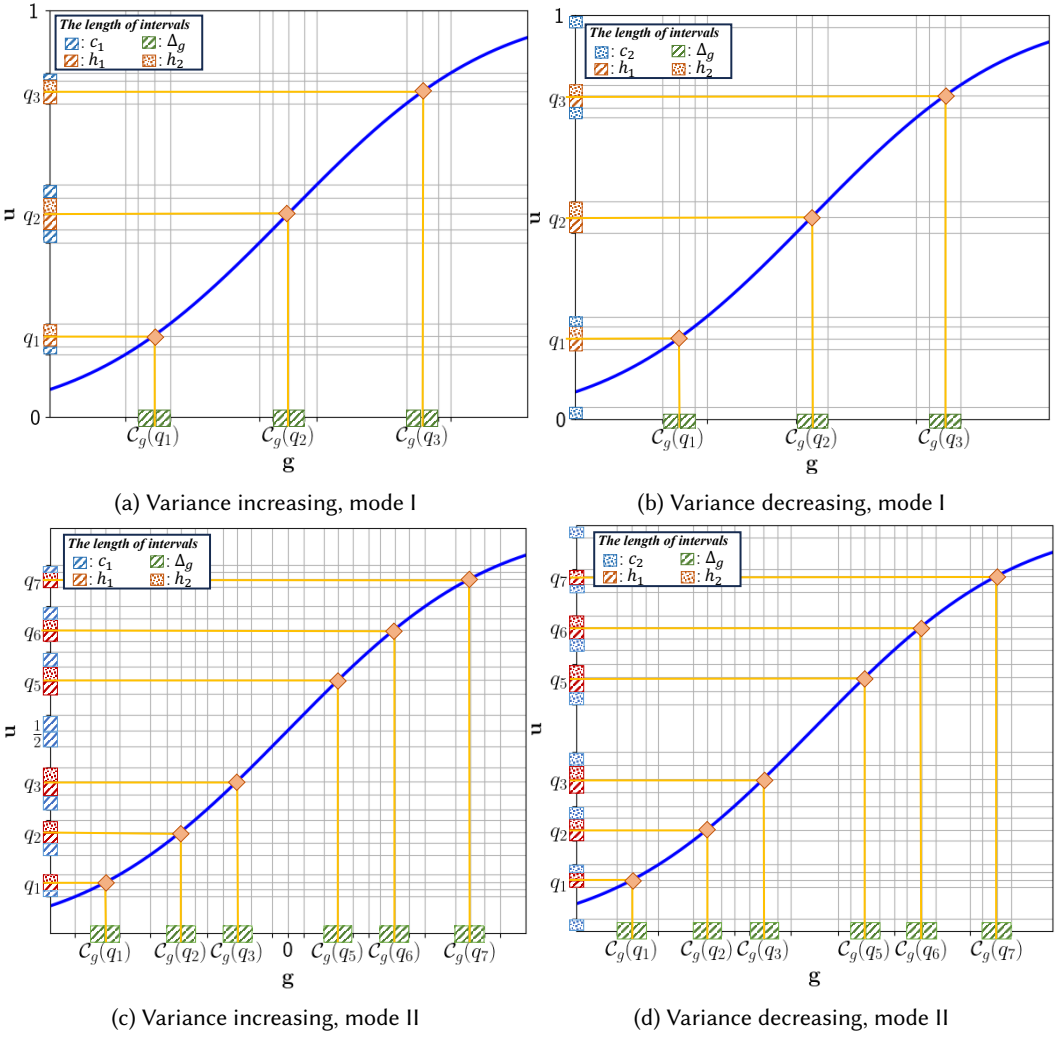


Fig. 1. Examples of $l = 2$ for modes I and II. Along the vertical axis in each figure, the red regions represent the neighborhoods of quantiles, and the blue regions represent the variance-correction intervals. Sampling within these regions is prohibited. The green regions are the intervals that we actually adjust. Our variance-preserving strategy in each iteration involves two key steps: (a) increasing S_u^2 by increasing c_1 , and (b) decreasing S_u^2 by increasing c_2 .

4.3 Adjustable PA-B2G

Section 4.2 demonstrates that PA-G2B can generate standard Gaussian noise and achieve provable security. However, in practical scenarios, numerical computation errors in ODE solvers and image quantization both significantly degrade message extraction accuracy. We observe that variations in u_i within the h -neighborhoods of the quantiles (defined in Theorem 4.2) are more likely to induce extraction errors. Therefore, we choose to slightly compromise the Gaussianity of g_s to improve message extraction accuracy.

One straightforward yet effective solution is to avoid sampling within these neighborhoods. According to [9], three conditions must be satisfied to achieve decent image generation performance: **i)** the sample mean of \mathbf{g}_s must be close to 0; **ii)** the sample variance of \mathbf{g}_s must be close to 1; **iii)** all entries of \mathbf{g}_s must be independent and identically distributed. Motivated by these requirements, we propose a variance-preserving algorithm. Before presenting further details, we state the following preliminary results.

THEOREM 4.2. *Let $\mathbf{q} = \{q_i | \frac{i}{2^l}, i = 1, \dots, 2^l - 1\}$ and $\tilde{\mathbf{q}} = \{\tilde{q}_i | \frac{i}{2^{l+1}}, i = 1, \dots, 2^{l+1} - 1, i \neq 2^l\}$ denote the quantile sets w.r.t. partitioning mode I and II, respectively. Assuming that sampling in the h -neighborhoods of these quantiles, which are expressed as $(q_i - h, q_i + h)$ for mode I and $(\tilde{q}_i - h, \tilde{q}_i + h)$ for mode II, is prohibited, we have $\bar{g} = \frac{1}{k} \sum_{i=1}^k g_i = 0$ and $S_g^2 = \frac{1}{k-1} \sum_{i=1}^k (g_i - \bar{g})^2 \neq 1$.*

PROOF. According to Theorem 4.1,

$$\begin{aligned} p(g) &= \sum_m p(g|C_u(m))p(C_u(m))p(m) \\ &= \frac{1}{2^l} \sum_m p(g|C_u(m))p(C_u(m)). \end{aligned} \quad (10)$$

For the mode I,

$$p(g) = \begin{cases} 0, & g \in \bigcup_{i=1}^{2^l-1} (C_g(q_i - h), C_g(q_i + h)). \\ \frac{2^l - h}{2^l \sqrt{2\pi}} e^{-\frac{g^2}{2}}, & g \in (-\infty, C_g(q_1 - h)) \cup (C_g(q_{2^l-1} + h), +\infty), \\ \frac{2^l - 2h}{2^l \sqrt{2\pi}} e^{-\frac{g^2}{2}}, & \text{otherwise.} \end{cases} \quad (11)$$

As for the mode II,

$$p(g) = \begin{cases} 0, & g \in \bigcup_{i=1, i \neq 2^l}^{2^{l+1}-1} (C_g(\tilde{q}_i - h), C_g(\tilde{q}_i + h)). \\ \frac{2^l - 2h}{2^l \sqrt{2\pi}} e^{-\frac{g^2}{2}}, & g \in (-\infty, C_g(\tilde{q}_1 - h)) \cup (C_g(\tilde{q}_{2^{l+1}-1} + h), +\infty) \\ \cup (C_g(\tilde{q}_{2^l-1} + h), C_g(\tilde{q}_{2^l+1} - h)), \\ \frac{2^l - 4h}{2^l \sqrt{2\pi}} e^{-\frac{g^2}{2}}, & \text{otherwise.} \end{cases} \quad (12)$$

According to Equation (11) and Equation (12), the following conclusions hold true for both modes I and II: **i)** $gp(g)$ is an odd function; **ii)** the integral interval is symmetric about the axis $g = 0$; and **iii)** the functions $gp(g)$ is bounded and contains a finite number of jump discontinuities within the integral interval. Collecting these conditions, we can derive that $E[g] = \int_{-\infty}^{\infty} gp(g)dg = 0$. According to the Law of Large Numbers, when $k \rightarrow \infty$, we have $E[g] = \bar{g} = 0$. Moreover, $D[g] = E[g^2] - (E[g])^2 = E[g^2] = \int_{-\infty}^{\infty} g^2 p(g)dg$. Clearly, according to Equation (11) and Equation (12), $D(g) = E[g^2] \neq 1$, and therefore, when $k \rightarrow \infty$, $D(g) = S_g^2 \neq 1$. \square

Theorem 4.2 indicates that the introduction of no-sampling intervals theoretically does not change the sample mean \bar{g} of \mathbf{g} , primarily due to the symmetry of our interval partitioning strategy proposed in Section 4.2. However, it induces a change in the sample variance S_g^2 . Therefore, we only need to correct S_g^2 to satisfy the three conditions mentioned above. To this end, we design a variance-preserving algorithm, whose essence lies in iteratively adjusting the sampling intervals of u to ensure that S_g^2 converges to 1. Specifically, if $S_g^2 > 1$, we iteratively reduce the sample variance S_u^2 of \mathbf{u} ; otherwise, we iteratively increase S_u^2 . Figure 1 shows two examples for $l = 2$ w.r.t. modes I and II, respectively, illustrating how S_u^2 is increased or decreased during each iteration. The complete implementation of our adjustable PA-B2G is given in Algorithm 3, and its reverse

Algorithm 3 Variance-Preserving Algorithm.**Input:** Secret message \mathbf{m} , maximum iteration steps N_{max} , and error tolerance e .**Output:** Sampling result \mathbf{g}_s .

```

1: Initialize  $c_1 = c_2 = 0$ ;
2: Generate a seed sequence  $s_1 \cdots s_k$ .
3: for  $i = 1$  to  $k$  do
4:   Sample  $r_i \sim \mathcal{U}(0, 1)$  with seed  $s_i$ ;
5:    $\triangleright$  mode I
6:    $h_1 = \frac{m_i+1}{2^l} - C_g^{-1}(C_g(\frac{m_i+1}{2^l}) - \Delta_g)$ ;
7:    $h_2 = C_g^{-1}(C_g(\frac{m_i}{2^l}) + \Delta_g) - \frac{m_i}{2^l}$ ;
8:    $u_i = (\frac{1}{2^l} - h_1 - h_2 - c_1 - c_2)r_i + \frac{m_i}{2^l} + h_2$ ;
9:    $u_i = u_i + c_1$  if  $\frac{m_i}{2} < \frac{1}{2}$  else  $u_i + c_2$ ;
10:   $\triangleright$  mode II
11:   $h_1 = \frac{(m_i+1) \bmod 2^l}{2^{l+1}} - C_g^{-1}(C_g(\frac{(m_i+1) \bmod 2^l}{2^{l+1}}) - \Delta_g)$ ;
12:   $h_2 = C_g^{-1}(C_g(\frac{m_i}{2^{l+1}}) + \Delta_g) - \frac{m_i}{2^{l+1}}$ ;
13:   $u_i = (\frac{1}{2^{l+1}} - h_1 - h_2 - c_1 - c_2)r_i + \frac{m_i}{2^{l+1}} + h_2 + c_1$  or  $u_i = (\frac{1}{2^{l+1}} - h_1 - h_2 - c_1 - c_2)r_i + 1 - \frac{m_i+1}{2^{l+1}} + h_2 + c_2$ ;
14: for  $step = 1$  to  $N_{max}$  do
15:    $\mathbf{g} = C_g(\mathbf{u})$  and calculate  $S_g^2$ ;
16:   if  $1 - S_g^2 > e$  then
17:      $c_1 = c_1 + \Delta_c$ ;
18:   else if  $S_g^2 - 1 > e$  then
19:      $c_2 = c_2 + \Delta_c$ ;
20:   else break;
21:   Repeat lines 3-13;
22: Return  $\mathbf{g}_s$ .
```

process is identical to that in Algorithm 2. Combining Algorithm 3 and Figure 1, we observe that MN, MB, MC, and Multi-bits [9] are in fact four special cases of our PA-B2G.

In Algorithm 3, we do not treat h as a hyperparameter; instead, we utilize Δ_g to dynamically determine the neighborhoods (referred to as no-sampling intervals) around each quantile. The rationale behind this is as follows: If we model the quantile as a continuous variable q , first, as $q \rightarrow 0$ or 1 , $C_g(q+h) - C_g(q-h)$ gradually increases, which significantly disrupts the Gaussianity of \mathbf{g} . Second, when $g = C_g(u)$ undergoes a small numerical perturbation Δ_g , we observe that $\Delta_u \approx \frac{dC_g^{-1}}{dg} \Delta_g$. Since C_g is the PPF of $\mathcal{N}(0, 1)$, $\frac{dC_g^{-1}}{dg}$ is a symmetric function that first increases and then decreases over its domain. Consequently, as $q \rightarrow 0$ or 1 , $\frac{dC_g^{-1}}{dg} \rightarrow 0$, leading to $\Delta_u \rightarrow 0$. This implies that overly long no-sampling intervals are unnecessary for $q \rightarrow 0$ or 1 . Based on this insight, we directly introduce a hyperparameter Δ_g to adjust the deviation of \mathbf{g} from $\mathcal{N}(\mathbf{0}, \mathbf{I})$, thereby enabling adaptive control over the length of the no-sampling intervals. As shown in fig. 1 and Theorem 4.2, for a given Δ_g , as $q \rightarrow 0$ or 1 , both h_1 and h_2 approach 0, which aligns seamlessly with our theoretical perspective.

4.4 Message Hiding and Extraction with PF-ODEs

After obtaining the noise \mathbf{g}_s via PA-B2G, \mathbf{g}_s can be reparameterized to accommodate selected diffusion models. The process of generating stego images from \mathbf{g}_s essentially amounts to a numerical

integration problem for ODEs. A variety of ODE solvers have been applied to diffusion models. In this paper, we primarily adopt the 2nd-order Heun solver [8] for stego image generation and initial noise retrieval for the following reasons: *i) Universality*: [8] provides a generalized ODE formulation that is compatible with most existing diffusion models using different noise schedulers (e.g., DDIM [23], VP-SDE [24], and VE-SDE [24]), without requiring additional training or fine-tuning. *ii) Efficiency*: Higher-order ODE solvers typically reduce local errors but also incur increased computational costs. 2nd-order Heun solver can achieve a favorable computational trade-off.

However, in practice, directly adapting the 2nd-order Heun solver to diffusion models defined over discretized timesteps may lead to numerical calculation errors. For instance, when adopting the noise scheduler of DDPM, we have $\sigma(t) = t = \sqrt{1 - \bar{\alpha}_t}$, where $\bar{\alpha}_t$ denotes a transformed noise scheduler defined in [4]. This gives rise to a critical issue: when attempting to retrieve \mathbf{g} from \mathbf{x}_0 , the Heun sampler fails because the initial noise parameter $\sigma(0) = \sqrt{1 - \bar{\alpha}_0} = 0$ (see the deterministic sampler defined in [8] for details). To resolve this problem, we propose retrieving \mathbf{g}_s from \mathbf{x}_ϵ instead of \mathbf{x}_0 , where ϵ is a small constant—for example, $\epsilon = 10^{-6}$ as employed in this paper. This modification does not affect the generation of stego images but effectively enhances the stability of message extraction.

5 Experiments

5.1 Experimental setup

Evaluation Metrics. We assess PA-B2G from four aspects: visual quality, steganographic security, message extraction accuracy, and embedding capacity.

- Visual quality is evaluated using the Fréchet Inception Distance (FID) score, computed across 50,000 stego images.
- Steganographic security is measured by detection accuracy (Acc_s) using the state-of-the-art steganalyzer UCNet [26], with 5,000 cover-stego image pairs for training and 1,000 pairs for testing. Note that the cover images are also generated by generative models but do not contain any hidden secret messages.
- Message extraction accuracy is measured by the average accuracy (\overline{Acc}), calculated over 1,000 stego images.
- Embedding capacity is measured in bits per pixel (bpp), calculated as $\frac{|b|}{h \times w}$, where h and w represent the image height and width, respectively.

Setup of PA-B2G. For low payloads, we automatically pad secret bit sequences with either 0 or 1 to match their length to the size of the generated images. For the following experiments, we set the maximum iteration steps $N_{max} = 100$ and the correction step size $\Delta_c = \frac{1}{3072}$.

5.2 Normality Test

We employ the one-sample Kolmogorov-Smirnov (K-S) test to assess the Gaussianity of samples generated by PA-B2G. For each sample, we test the null hypothesis H_0 , which posits that the sample follows $\mathcal{N}(0, 1)$, against the alternative hypothesis H_1 . A p -value below 0.05 leads to the rejection of H_0 ; otherwise, it is accepted. Through a random generation process, we create 1,000 samples and compute the ratio $N_{H_0}/1,000$, where N_{H_0} denotes the number of samples for which H_0 is accepted. Section 5.1 shows the test results *w.r.t.* varying $\Delta_g \in \{0, 0.02\}$ and payloads of 3 bpp, 6 bpp, and 9 bpp for both modes I and II.

As observed, when no-sampling intervals are not introduced (*i.e.*, $\Delta_g = 0$), the samples generated by PA-B2G for any noise size and payload almost strictly adhere to $\mathcal{N}(0, 1)$. However, even though Δ_g is a small value, the ratio $N_{H_0}/1,000$ decreases significantly, particularly for large noise sizes. This may occur because the normality of samples generated by PA-B2G is highly sensitive to Δ_g , while,

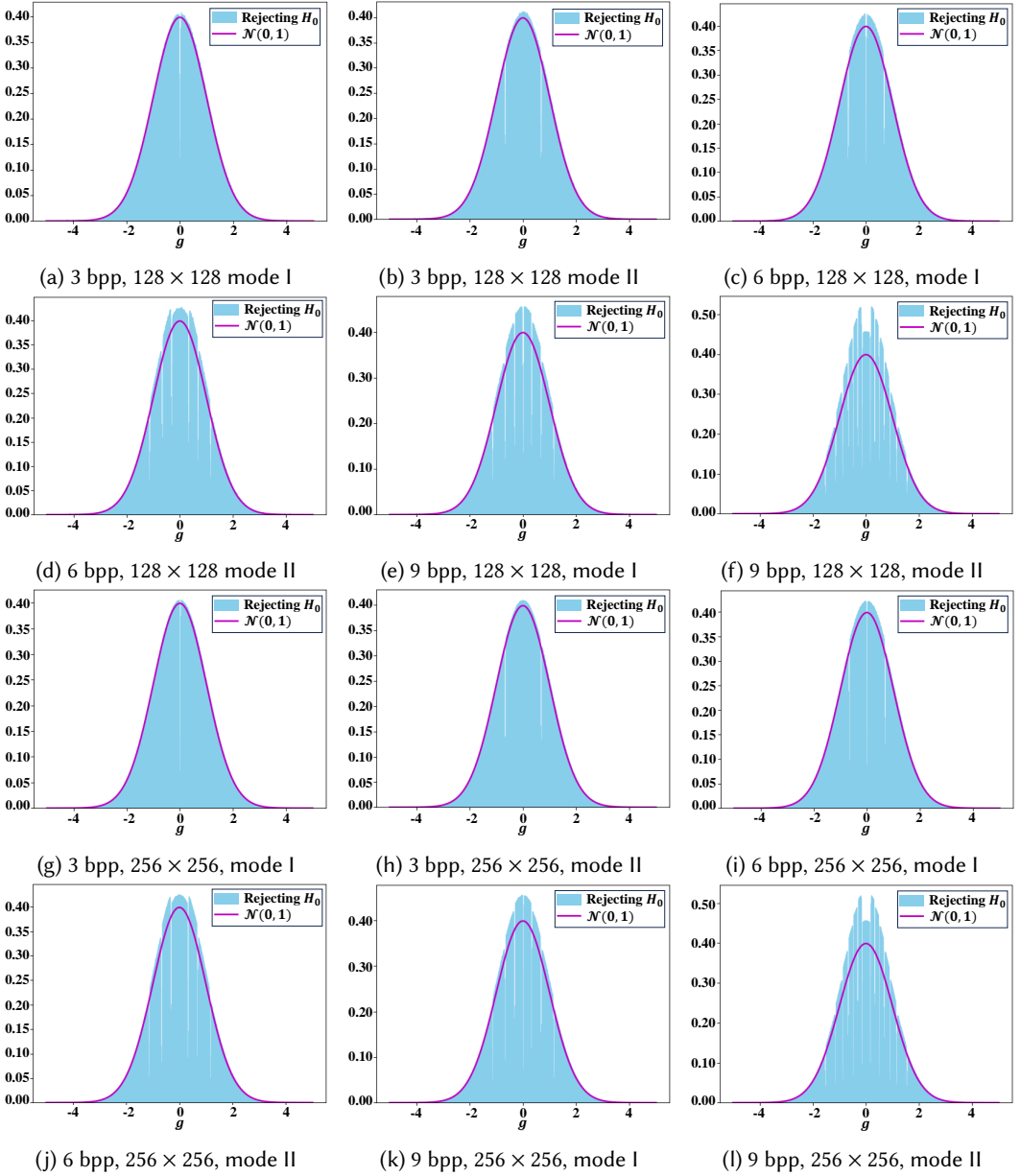


Fig. 2. Averaged histograms of noise that rejecting H_0 w.r.t. different payloads and noise sizes under $\Delta_g = 0.02$.

conversely, the sensitivity of the K-S test improves as the sample scale increases. Furthermore, we depict the averaged histograms of noise samples that reject H_0 at varying payloads and noise sizes for $\Delta_g = 0.02$ in Figure 2. As illustrated, as the payload increases, the distribution of g_s gradually deviates from $\mathcal{N}(0, 1)$. However, for low payloads, even when H_0 is rejected, these histograms still closely resemble the distribution of noise sampled from $\mathcal{N}(0, 1)$.

Table 1. Normality test of samples generated by PA-B2G in modes I and II with four different sample sizes w.r.t. varying payloads and Δ_g .

Noise Size($\times 3$)	3 bpp		6 bpp		9 bpp		
	Mode I	Mode II	Mode I	Mode II	Mode I	Mode II	
$\Delta_g = 0.00$	32×32	0.957	0.952	0.959	0.954	0.952	0.951
	64×64	0.949	0.947	0.951	0.952	0.948	0.950
	128×128	0.947	0.949	0.947	0.953	0.950	0.945
	256×256	0.946	0.950	0.949	0.951	0.951	0.948
$\Delta_g = 0.02$	32×32	0.849	0.872	0.835	0.844	0.845	0.795
	64×64	0.405	0.601	0.431	0.401	0.393	0.333
	128×128	0.00	0.00	0.00	0.00	0.00	0.00
	256×256	0.00	0.00	0.00	0.00	0.00	0.00

Table 2. Comparison with existing message mapping methods using metrics FID, Acc_s , and \overline{Acc} on CIFAR-10 32×32 , FFHQ 64×64 , and LSUN-Bedroom 256×256 datasets under different payloads. PA-B2G¹(.00) denotes PA-B2G in mode I with $\Delta_g = 0.00$, and others follow similarly.

Method	CIFAR-10 32×32						FFHQ 64×64						LSUN-Bedroom 256×256					
	3 bpp			6bpp			3 bpp			6 bpp			3 bpp			6 bpp		
	FID↓	\overline{Acc} ↑	Acc_s ↓	FID↓	\overline{Acc} ↑	Acc_s ↓	FID↓	\overline{Acc} ↑	Acc_s ↓	FID↓	\overline{Acc} ↑	Acc_s ↓	FID↓	\overline{Acc} ↑	Acc_s ↓	FID↓	\overline{Acc} ↑	Acc_s ↓
MN [9]	2.02	83.86%	50.60%	-	-	-	2.46	86.22%	50.83%	-	-	-	10.21	79.46%	49.95%	-	-	-
MB [9]	2.64	94.36%	92.35%	-	-	-	4.16	98.12%	99.70%	-	-	-	10.98	96.89%	99.90%	-	-	-
MC [9]	2.25	84.96%	67.00%	-	-	-	3.10	92.70%	97.15%	-	-	-	10.82	82.39%	99.20%	-	-	-
Multi-bits [9]	-	-	-	2.37	83.01%	74.80%	-	-	-	3.30	90.57%	98.85%	-	-	-	10.90	80.90%	99.90%
GSD [35]	2.98	98.89%	64.54%	-	-	-	3.08	98.81%	50.24%	-	-	-	10.89	94.11%	50.56%	-	-	-
GS [31]	1.99	84.50%	50.94%	2.01	74.98%	50.12%	2.42	86.24%	50.35%	2.45	79.98%	50.54%	10.21	79.84%	50.74%	10.22	72.04%	50.15%
PA-B2G ¹ (.00)	1.97	84.10%	50.49%	2.03	75.60%	50.75%	2.45	86.85%	50.58%	2.46	79.25%	50.65%	10.19	79.46%	49.74%	10.20	71.12%	49.50%
PA-B2G ¹ (.08)	2.19	88.16%	56.30%	2.17	80.02%	56.82%	2.95	92.76%	79.95%	2.98	88.40%	79.85%	10.75	86.10%	72.75%	10.78	78.10%	72.35%
PA-B2G ² (.00)	2.01	75.64%	50.75%	2.00	69.11%	50.43%	2.40	79.22%	50.43%	2.43	70.90%	50.55%	10.21	72.14%	48.80%	10.21	62.54%	49.80%
PA-B2G ² (.08)	2.13	80.99%	53.80%	2.08	71.53%	53.40%	2.94	88.35%	79.50%	2.89	77.16%	79.60%	10.71	82.87%	71.80%	10.73	71.90%	72.30%

Table 3. Comparison with GAN-based and Flow-based GS methods using metrics FID, Acc_s , and \overline{Acc} on CelebA 64×64 under various payloads. PA-B2G¹(.08) denotes PA-B2G in mode I with $\Delta_g = 0.08$.

Method	3 bpp			6 bpp			9 bpp		
	FID↓	\overline{Acc} ↑	Acc_s ↓	FID↓	\overline{Acc} ↑	Acc_s ↓	FID↓	\overline{Acc} ↑	Acc_s ↓
GSF[28]	25.02	91.98%	51.87%	44.17	73.47%	99.73%	51.80	62.85%	99.87%
GSN[27]	16.11	74.31%	99.80%	17.02	60.75%	99.47%	19.98	52.25%	99.54%
S2IRT[37]	44.52	50.10%	50.85%	45.74	50.47%	50.12%	-	-	-
PA-B2G ¹ (.08)	7.70	90.81%	76.75%	7.68	80.89%	76.54%	7.72	72.88%	76.12%

5.3 Method Comparison

Comparison with Prior DM-GIS Methods. We compare PA-B2G with message mapping methods including MN, MB, MC, and Multi-bits proposed in [9], GSD [29], and Gaussian Shading (GS) [31].

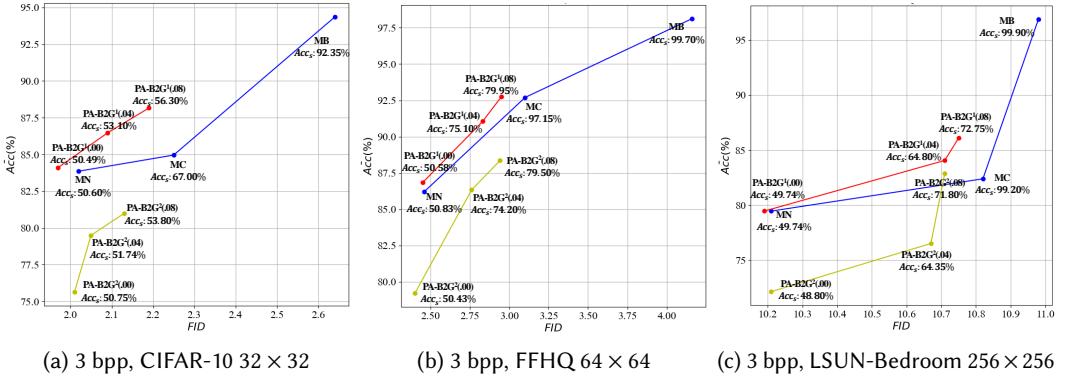


Fig. 3. Visualization results of the adjustment strategies adopted by [9] and PA-B2G on CIFAR-10, FFHQ, and LSUN-Bedroom.

All message mapping methods are evaluated on CIFAR-10 32×32 , FFHQ 64×64 , and LSUN-Bedroom 256×256 datasets. For each dataset, we equip each mapping method with the same generative backbone and sampling scheduler. Specifically, we employ the 2nd order Heun ODE solver with 20 sampling steps on CIFAR-10 32×32 and with 42 sampling steps on FFHQ 64×64 , while using the 1st order ODE solver proposed in DDIM [23] with 18 sampling steps on LSUN-Bedroom 256×256 . We set the error tolerance $e = 0.0185$ defined in Algorithm 3 for CIFAR-10 32×32 and FFHQ 64×64 , and $e = 0.007$ for LSUN-Bedroom 256×256 . Before message hiding, we pad all secret bits and then encrypt them to meet required payloads. All mapping methods utilize the same random seed for stego image generation, and the corresponding generated images are saved in PNG format. Note that the payloads listed in Section 5.3 are effective payloads.

We list the FID score, average message extraction accuracy \overline{Acc}_e , and detection accuracy Acc_d for each method across various payloads in Section 5.3. MN, GS, and PA-B2G with $\Delta_g = 0$ achieve optimal stego image quality and perfect security by generating pure Gaussian noise; however, this comes at the expense of reduced message extraction accuracy. Furthermore, GSD suffers from deteriorated visual quality and security in low-resolution (e.g., 32×32) scenarios, because the Central Limit Theorem fails in low-dimensional spaces, causing the noise \mathbf{g}_s to deviate from a standard Gaussian distribution. However, as dimension increases, this problem is gradually alleviated. Despite achieving state-of-the-art extraction accuracy, GSD’s constrained embedding capacity (3 bpp maximum) limits its practical use in steganography. Alternatively, MB, MC, and Multi-bits fail to maintain their claimed security when evaluated against [26], with detection accuracies often exceeding 95% at high payloads due to significantly compromised Gaussianity. These methods also lack flexibility for varying payloads. Conversely, PA-B2G adapts flexibly between low and high payloads. It maintains comparable image quality and security by tuning Δ_g with minimal impact on extraction accuracy. Notably, the inclusion of additional quantiles in PA-B2G mode II leads to a decrease in message extraction accuracy relative to mode I, rendering the latter more robust for real-world deployment.

Comparison with GAN- and Flow-based Methods. We also compare PA-B2G with two flow-based methods, GSF [28] and S2IRT [37], and a GAN-based method, GSN [27], on the CelebA 64×64 dataset with payloads ranging from 3 to 9 bpp. GSF and S2IRT utilize the same pre-trained Glow model¹. For S2IRT, to maintain computational efficiency, we set the group number K to 30 for a

¹<https://github.com/rosinality/glow-pytorch>

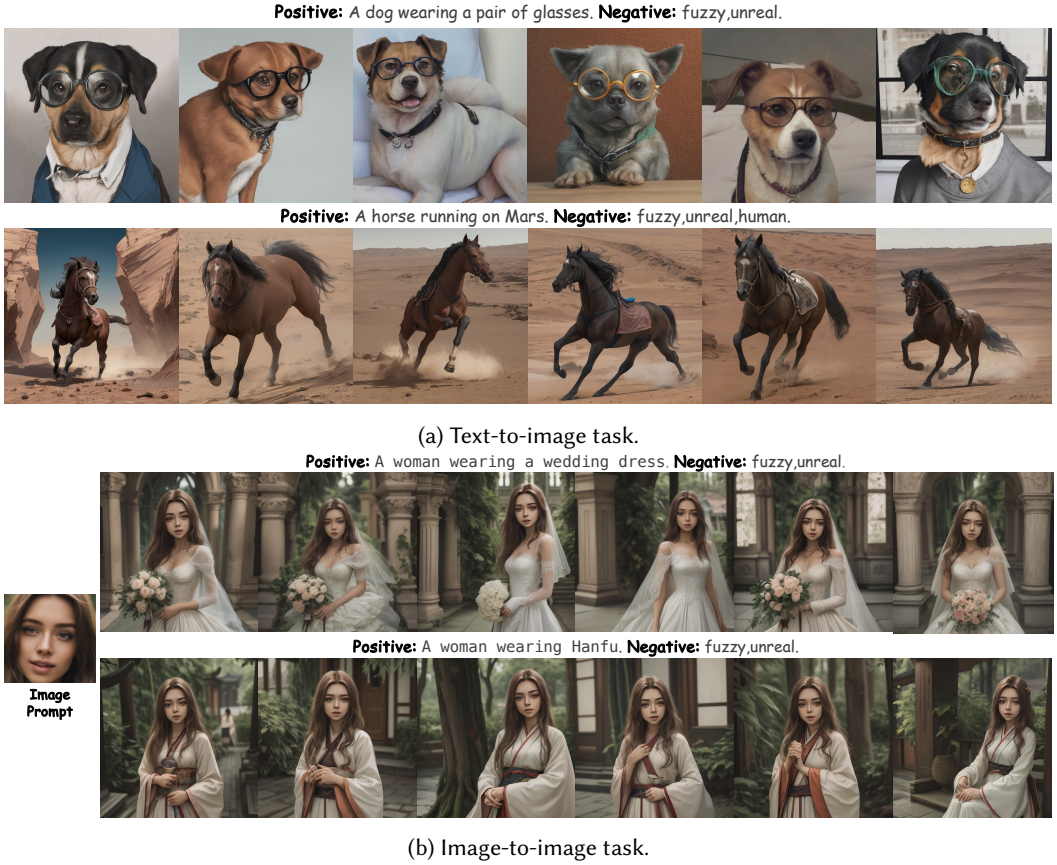


Fig. 4. Visualization results of combining PA-B2G in mode I with Stable Diffusion on text-to-image and image-to-image tasks.

3 bpp payload and to 40 for 6 bpp. At higher payloads, S2IRT requires a larger K , making it too time-consuming to generate 50,000 stego images; thus, we do not report its corresponding results in Section 5.3. Given that PA-B2G in Mode I is superior to Mode II in extraction accuracy, we select it with $\Delta_g = 0.08$ and $e = 0.007$ for comparison. We employ the pre-trained diffusion model from DDIM [23] but replace its sampling scheduler with the Heun ODE solver, as suggested in Section 4.4. As shown in Section 5.3, PA-B2G significantly outperforms GAN- and flow-based methods, particularly in image quality and message extraction accuracy, primarily due to the powerful generation capabilities of diffusion models and our provable, adjustable message mapping. Regarding security, S2IRT achieves the best anti-detectability, as the extra perturbation key it introduces ensures that the generated noise strictly follows a pure Gaussian distribution. In contrast, GSF and GSN alter the noise distribution and are thus easily detected by UCNet.

Comparison with Prior Adjustment Strategies. Kim *et al.* [9] identify a trade-off between stego image quality and extraction accuracy, proposing MN, MB, and MC as balancing options. To evaluate our adjustment strategy (Algorithm 3), Section 5.3 reports the FID score, \overline{Acc} , and Acc_s for these methods alongside PA-B2G (modes I & II) across varying Δ_g . For better intuition, Figure 3 illustrates further adjustment results, confirming that image quality, security, and accuracy can be

Table 4. Robustness evaluation of average message extraction accuracy (%) under various image distortions (JPEG compression with different quality factors, random cropping with varying ratios, Gaussian noise with varying standard deviations, and Gaussian blurring with varying radii) across different payload sizes (256, 512, and 1024 bits)

Payload	JPEG			Random Crop			Gaussian Noise			Gaussian Blur		
	90	75	50	0.1	0.3	0.5	0.01	0.03	0.05	2	3	4
256 bits	100.00%	99.89%	99.46%	99.98%	99.04%	87.05%	99.85%	98.03%	94.45%	99.94%	99.25%	96.64%
512 bits	99.80%	99.27%	98.20%	99.51%	94.20%	78.25%	98.79%	94.95%	85.58%	99.26%	96.58%	91.48%
1024 bits	98.60%	97.30%	94.45%	97.48%	87.88%	71.22%	96.64%	88.86%	81.93%	96.04%	90.76%	83.43%

effectively balanced by tuning Δ_g . This supports our analysis in Section 4.1 and reveals that Mode I provides a more natural, fine-grained adjustment than [9]. By modulating Δ_g , PA-B2G can readily match the performance of MN, MB, and MC, as they represent special cases of our generalized framework.

5.4 Diffusion Model Watermarking

In this section, we further validate the effectiveness of PA-B2G in model I for watermarking diffusion models. We employ Dreamshaper 7, which is fine-tuned on Stable Diffusion 1.5, as the generative backbone, and utilize a first-order DDIM solver with 50 sampling steps for stego image generation. We evaluate three effective payloads—256, 512, and 1024 bits—and report their corresponding average message extraction accuracy (\overline{Acc}) over 1000 stego images against various lossy processing techniques in Section 5.4. These techniques include JPEG compression with different quality factors, random cropping with varying ratios, Gaussian noise with varying standard deviations, and Gaussian blurring with varying radii. For PA-B2G, the error tolerance e is set to 0.02, code length l to 1, and Δ_g to 0.05.

As reported in Section 5.4, PA-B2G exhibits robust resistance to nearly all lossy processing when the effective payload is 256 bits. Notably, even with a cropping ratio of 0.5, PA-B2G still guarantees an extraction accuracy of 87.05%. While the extraction accuracy gradually decreases as the payload increases, PA-B2G with a 1024-bit payload still effectively resists JPEG compression ($\overline{Acc} > 94\%$), which is a common operation on social media platforms. In addition to extraction accuracy, we present the visual generation results for text-to-image and image-to-image tasks in Figure 4. As shown, the stego images produced by PA-B2G exhibit visual quality indistinguishable from normally generated images. These experimental results demonstrate that PA-B2G can be effectively extended to the watermarking of diffusion models.

5.5 Computational Complexity

This section evaluates the computational complexity of PA-B2G in modes I and II. The complete message-hiding pipeline encompasses four stages: mapping the secret bit sequence \mathbf{b} to noise \mathbf{g}_s , reverse ODE solving, forward ODE solving, and recovering \mathbf{b} from \mathbf{g}_s . Section 5.4 presents the average execution time for the initial mapping stage, with the error tolerance e set to 0.0185. While the computational overhead scales with noise dimensionality and Δ_g , it can be mitigated by increasing the correction step Δ_c or error tolerance e . Notably, PA-B2G consistently completes this initial mapping in one second, regardless of the mode or noise dimensions. While the time consumption of the ODE solving processes also depends on specific diffusion architectures and sampling steps, it is considered beyond the scope of this paper. The time required for message recovery is marginal compared to the mapping process and is thus omitted.

Table 5. Average time required to generate noise g_s of different sizes using PA-B2G in modes I and II with varying Δ_g .

Method	32×32×3		64×64×3		128×128×3	
	3 bpp	6 bpp	3 bpp	6 bpp	3 bpp	6 bpp
PA-B2G ¹ (.00)	0.004s	0.005s	0.015s	0.016s	0.061s	0.084s
PA-B2G ¹ (.04)	0.018s	0.022s	0.054s	0.089s	0.193s	0.306s
PA-B2G ¹ (.08)	0.043s	0.049s	0.148s	0.222s	0.520s	0.871s
PA-B2G ² (.00)	0.005s	0.007s	0.025s	0.029s	0.084s	0.119s
PA-B2G ² (.04)	0.020s	0.025s	0.071s	0.074s	0.217s	0.264s
PA-B2G ² (.08)	0.046s	0.057s	0.171s	0.177s	0.725s	0.784s

6 Conclusion

We analyze the inherent trade-off among stego-image quality, steganographic security, and message extraction accuracy in DM-GIS. Based on this analysis, we propose PA-B2G, a provably invertible bit-to-Gaussian mapping. By integrating with off-the-shelf diffusion models, PA-B2G can establish a theoretically invertible transform between secret bitstreams and stego images. Experimental results demonstrate that our DM-GIS approach supports arbitrary-length payloads while achieving highly competitive performance in image quality, security, and extraction accuracy. Furthermore, its robustness against lossy processing in watermarking applications validates its practical effectiveness. In future work, we plan to extend PA-B2G to broader diffusion-based generation tasks, such as video generation.

References

- [1] Tomáš Filler, Jan Judas, and Jessica Fridrich. 2011. Minimizing additive distortion in steganography using syndrome-trellis codes. *IEEE Transactions on Information Forensics and Security* 6, 3 (2011), 920–935.
- [2] Jessica Fridrich and Jan Kodovsky. 2012. Rich models for steganalysis of digital images. *IEEE Transactions on Information Forensics and Security* 7, 3 (2012), 868–882.
- [3] Ian Goodfellow, Jean Pouget-Abadie, Mehdi Mirza, Bing Xu, David Warde-Farley, Sherjil Ozair, Aaron Courville, and Yoshua Bengio. 2020. Generative adversarial networks. *Commun. ACM* 63, 11 (2020), 139–144.
- [4] Jonathan Ho, Ajay Jain, and Pieter Abbeel. 2020. Denoising diffusion probabilistic models. *Advances in neural information processing systems* 33 (2020), 6840–6851.
- [5] Donghui Hu, Liang Wang, Wenjie Jiang, Shuli Zheng, and Bin Li. 2018. A novel image steganography method via deep convolutional generative adversarial networks. *IEEE access* 6 (2018), 38303–38314.
- [6] Kun Hu, Mingpei Wang, Xiaohui Ma, Jia Chen, Xiaochao Wang, and Xingjun Wang. 2024. Learning-based image steganography and watermarking: A survey. *Expert Systems with Applications* 249 (2024), 123715.
- [7] Xiaoxiao Hu, Sheng Li, Qichao Ying, Wanli Peng, Xinpeng Zhang, and Zhenxing Qian. 2024. Establishing robust generative image steganography via popular stable diffusion. *IEEE Transactions on Information Forensics and Security* 19 (2024), 8094–8108.
- [8] Tero Karras, Miika Aittala, Timo Aila, and Samuli Laine. 2022. Elucidating the design space of diffusion-based generative models. *Advances in Neural Information Processing Systems* 35 (2022), 26565–26577.
- [9] Daegyu Kim, Chaehun Shin, Jooyoung Choi, Dahyun Jung, and Sungroh Yoon. 2025. Diffusion-stego: Training-free diffusion generative steganography via message projection. *Information Sciences* 718 (2025), 122358.
- [10] Durk P Kingma and Prafulla Dhariwal. 2018. Glow: Generative flow with invertible 1x1 convolutions. *Advances in neural information processing systems* 31 (2018).
- [11] Chieh-Hsin Lai, Yang Song, Dongjun Kim, Yuki Mitsufuji, and Stefano Ermon. 2025. The principles of diffusion models. *arXiv preprint arXiv:2510.21890* (2025).
- [12] Ming-ming Liu, Min-qing Zhang, Jia Liu, Ying-nan Zhang, and Yan Ke. 2017. Coverless information hiding based on generative adversarial networks. *arXiv preprint arXiv:1712.06951* (2017).

- [13] Xiyao Liu, Ziping Ma, Junxing Ma, Jian Zhang, Gerald Schaefer, and Hui Fang. 2022. Image disentanglement autoencoder for steganography without embedding. In *Proceedings of the IEEE/CVF conference on computer vision and pattern recognition*. 2303–2312.
- [14] Cheng Lu, Yuhao Zhou, Fan Bao, Jianfei Chen, Chongxuan Li, and Jun Zhu. 2022. Dpm-solver: A fast ode solver for diffusion probabilistic model sampling in around 10 steps. *Advances in neural information processing systems* 35 (2022), 5775–5787.
- [15] Cheng Lu, Yuhao Zhou, Fan Bao, Jianfei Chen, Chongxuan Li, and Jun Zhu. 2025. Dpm-solver++: Fast solver for guided sampling of diffusion probabilistic models. *Machine Intelligence Research* 22, 4 (2025), 730–751.
- [16] Weiqi Luo, Fangjun Huang, and Jiwu Huang. 2010. Edge adaptive image steganography based on LSB matching revisited. *IEEE Transactions on information forensics and security* 5, 2 (2010), 201–214.
- [17] Ziping Ma, Yuesheng Zhu, Guibo Luo, Xiyao Liu, Gerald Schaefer, and Hui Fang. 2023. Robust Steganography without Embedding Based on Secure Container Synthesis and Iterative Message Recovery. In *IJCAI*. 4838–4846.
- [18] Yinyin Peng, Donghui Hu, Yaofei Wang, Kejiang Chen, Gang Pei, and Weiming Zhang. 2023. StegaDDPM: Generative Image Steganography based on Denoising Diffusion Probabilistic Model. In *Proceedings of the 31st ACM International Conference on Multimedia*. 7143–7151.
- [19] Aditya Ramesh, Prafulla Dhariwal, Alex Nichol, Casey Chu, and Mark Chen. 2022. Hierarchical text-conditional image generation with clip latents. *arXiv preprint arXiv:2204.06125* 1, 2 (2022), 3.
- [20] Robin Rombach, Andreas Blattmann, Dominik Lorenz, Patrick Esser, and Björn Ommer. 2022. High-resolution image synthesis with latent diffusion models. In *Proceedings of the IEEE/CVF conference on computer vision and pattern recognition*. 10684–10695.
- [21] Chitwan Saharia, William Chan, Saurabh Saxena, Lala Li, Jay Whang, Emily Denton, Seyed Kamyar Seyed Ghasemipour, Burcu Karagol Ayan, S. Sara Mahdavi, Rapha Gontijo Lopes, Tim Salimans, Jonathan Ho, David J Fleet, and Mohammad Norouzi. 2022. Photorealistic Text-to-Image Diffusion Models with Deep Language Understanding. *arXiv:2205.11487* [cs.CV] <https://arxiv.org/abs/2205.11487>
- [22] Bingbing Song, Ping Wei, Sixing Wu, Yu Lin, and Wei Zhou. 2024. A survey on deep-learning-based image steganography. *Expert Systems with Applications* 254 (2024), 124390.
- [23] Jiaming Song, Chenlin Meng, and Stefano Ermon. 2020. Denoising Diffusion Implicit Models. In *International Conference on Learning Representations*.
- [24] Yang Song, Jascha Sohl-Dickstein, Diederik P Kingma, Abhishek Kumar, Stefano Ermon, and Ben Poole. 2020. Score-Based Generative Modeling through Stochastic Differential Equations. In *International Conference on Learning Representations*.
- [25] Zihan Wang, Neng Gao, Xin Wang, Xuexin Qu, and Linghui Li. 2018. SSteGAN: self-learning steganography based on generative adversarial networks. In *Neural Information Processing: 25th International Conference, ICONIP 2018, Siem Reap, Cambodia, December 13–16, 2018, Proceedings, Part II 25*. Springer, 253–264.
- [26] Kangkang Wei, Weiqi Luo, Shunquan Tan, and Jiwu Huang. 2022. Universal Deep Network for Steganalysis of Color Image Based on Channel Representation. *IEEE Transactions on Information Forensics and Security* 17 (2022), 3022–3036. [doi:10.1109/TIFS.2022.3196265](https://doi.org/10.1109/TIFS.2022.3196265)
- [27] Ping Wei, Sheng Li, Xinpeng Zhang, Ge Luo, Zhenxing Qian, and Qing Zhou. 2022. Generative steganography network. In *Proceedings of the 30th ACM International Conference on Multimedia*. 1621–1629.
- [28] Ping Wei, Ge Luo, Qi Song, Xinpeng Zhang, Zhenxing Qian, and Sheng Li. 2022. Generative steganographic flow. In *2022 IEEE International Conference on Multimedia and Expo*. IEEE, 1–6.
- [29] Ping Wei, Qing Zhou, Zichi Wang, Zhenxing Qian, Xinpeng Zhang, and Sheng Li. 2023. Generative Steganography Diffusion. *arXiv preprint arXiv:2305.03472* (2023).
- [30] Guanshuo Xu, Han-Zhou Wu, and Yun-Qing Shi. 2016. Structural design of convolutional neural networks for steganalysis. *IEEE Signal Processing Letters* 23, 5 (2016), 708–712.
- [31] Zijin Yang, Kai Zeng, Kejiang Chen, Han Fang, Weiming Zhang, and Nenghai Yu. 2024. Gaussian shading: Provable performance-lossless image watermarking for diffusion models. In *Proceedings of the IEEE/CVF Conference on Computer Vision and Pattern Recognition*. 12162–12171.
- [32] WeiKe You, Hong Zhang, and Xianfeng Zhao. 2020. A Siamese CNN for image steganalysis. *IEEE Transactions on Information Forensics and Security* 16 (2020), 291–306.
- [33] Cong Yu, Donghui Hu, Shuli Zheng, Wenjie Jiang, Meng Li, and Zhong-qiu Zhao. 2021. An improved steganography without embedding based on attention GAN. *Peer-to-Peer Networking and Applications* 14 (2021), 1446–1457.
- [34] Kaiwen Zheng, Cheng Lu, Jianfei Chen, and Jun Zhu. 2023. Dpm-solver-v3: Improved diffusion ode solver with empirical model statistics. *Advances in Neural Information Processing Systems* 36 (2023), 55502–55542.
- [35] Qing Zhou, Ping Wei, Zhenxing Qian, Xinpeng Zhang, and Sheng Li. 2025. Improved generative steganography based on diffusion model. *IEEE Transactions on Circuits and Systems for Video Technology* (2025).

- [36] Zhili Zhou, Xiaohua Dong, Ruohan Meng, Meimin Wang, Hongyang Yan, Keping Yu, and Kim-Kwang Raymond Choo. 2023. Generative Steganography via Auto-Generation of Semantic Object Contours. *IEEE Transactions on Information Forensics and Security* (2023).
- [37] Zhili Zhou, Yuecheng Su, Jin Li, Keping Yu, QM Jonathan Wu, Zhangjie Fu, and Yunqing Shi. 2022. Secret-to-image reversible transformation for generative steganography. *IEEE Transactions on Dependable and Secure Computing* (2022).
- [38] Jiahao Zhu, Zixuan Chen, Jiali Liu, Lingxiao Yang, Yi Zhou, Weiqi Luo, and Xiaohua Xie. 2026. Rethinking Security of Diffusion-based Generative Steganography. *arXiv preprint arXiv:2602.10219* (2026).